



Published in final edited form as:

*J Mol Cell Cardiol.* 2020 February ; 139: 238–249. doi:10.1016/j.yjmcc.2020.02.002.

## Diaphragm weakness and proteomics (global and redox) modifications in heart failure with reduced ejection fraction in rats

Rachel C. Kelley<sup>1</sup>, Brian McDonagh<sup>2</sup>, Babette Brumback<sup>3</sup>, Glenn A. Walter<sup>4</sup>, Ravneet Vohra<sup>4</sup>, Leonardo F. Ferreira<sup>1</sup>

<sup>1</sup>Department of Applied Physiology and Kinesiology, University of Florida, Gainesville, FL.

<sup>2</sup>Department of Physiology, National University of Ireland, Galway, Ireland. <sup>3</sup>Department of Biostatistics, University of Florida, Gainesville, FL. <sup>4</sup>Department of Physiology and Functional Genomics, University of Florida, Gainesville, FL

### Abstract

Inspiratory dysfunction occurs in patients with heart failure with reduced ejection fraction (HFrEF) in a manner that depends on disease severity and by mechanisms that are not fully understood. In the current study, we tested whether HFrEF effects on diaphragm (inspiratory muscle) depend on disease severity and examined putative mechanisms for diaphragm abnormalities via global and redox proteomics. We allocated male rats into Sham, moderate (mHFrEF), or severe HFrEF (sHFrEF) induced by myocardial infarction and examined the diaphragm muscle. Both mHFrEF and sHFrEF caused atrophy in type IIa and IIb/x fibers. Maximal and twitch specific forces (N/cm<sup>2</sup>) were decreased by 19±10% and 28±13%, respectively, in sHFrEF ( $p < 0.05$ ), but not in mHFrEF. Global proteomics revealed upregulation of sarcomeric proteins and downregulation of ribosomal and glucose metabolism proteins in sHFrEF. Redox proteomics showed that sHFrEF increased reversibly oxidized cysteine in cytoskeletal and thin filament proteins and methionine in skeletal muscle  $\alpha$ -actin (range 0.5 to 3.3-fold;  $p < 0.05$ ). In conclusion, fiber atrophy plus contractile dysfunction caused diaphragm weakness in HFrEF. Decreased ribosomal proteins and heightened reversible oxidation of protein thiols are candidate mechanisms for atrophy or anabolic resistance as well as loss of specific force in sHFrEF.

**Corresponding author:** Leonardo F. Ferreira, PhD, Department of Applied Physiology and Kinesiology, University of Florida, 1864 Stadium Rd, room 100 FLG, Gainesville, FL, 32611-8205, ferreira@hhp.ufl.edu, +1 (352) 294-1724.

#### Author contributions

Conception and design of the experiments: R.C.K., B.M., and L.F.F. Collection and analysis of data: R.C.K., B.M., B.B., G.A.W., R.V., and L.F.F. Interpretation of data: R.C.K., B.M., B.B., G.A.W., R.V., and L.F.F. Drafting the article: R.C.K., B.M., and L.F.F. Critical revision of article for intellectual content: R.C.K., B.M., B.B., G.A.W., R.V., and L.F.F. All authors read and approved the manuscript before submission. All persons designated as authors qualify for authorship, and all those who qualify for authorship are listed. All authors agree to be accountable for all aspects of the work in ensuring that questions related to the accuracy or integrity of any part of the work are appropriately investigated and resolved.

#### Disclosures

None.

**Publisher's Disclaimer:** This is a PDF file of an unedited manuscript that has been accepted for publication. As a service to our customers we are providing this early version of the manuscript. The manuscript will undergo copyediting, typesetting, and review of the resulting proof before it is published in its final form. Please note that during the production process errors may be discovered which could affect the content, and all legal disclaimers that apply to the journal pertain.

## Keywords

methionine; cysteine; oxidation; muscle atrophy; muscle force

## 1. Introduction

As the main inspiratory muscle, the diaphragm is essential in ventilatory and non-ventilatory behaviors (1). Patients with heart failure who have reduced ejection fraction (HFrEF) show a decline in maximal inspiratory pressure, which is an indirect marker of diaphragm force/function (2, 3). *Maximal inspiratory pressure is an independent predictor of prognosis in patients with HFrEF* (4, 5). *Patient data and direct measurement of diaphragm abnormalities in rodent models of HFrEF suggest that dysfunction of this respiratory muscle contributes to the pathophysiology of HFrEF* (3). *In general, diaphragm dysfunction leads to impaired airway clearance and predisposition to pneumonia, inability to sustain ventilation and shallow breathing that limits gas exchange during physical activity, and reflex sympathetic activation, which vasoconstricts the periphery as well as exacerbates pathological cardiac remodeling* (3, 6). *These physiological changes worsen patient symptoms of dyspnea and discomfort, and can accelerate disease progression.* Therefore, it is important to resolve the underlying mechanisms of diaphragm dysfunction and develop new therapies for patients with HFrEF.

Assuming a maximal voluntary effort and sufficient neuromuscular transmission, the decrease in maximal inspiratory pressure in patients is the result of diaphragm fiber atrophy and contractile dysfunction. In animal models of HFrEF, some studies support and others refute the existence of diaphragm atrophy or contractile dysfunction (7–12). The decline in maximal inspiratory pressure in patients depends on disease severity (3, 13). Thus, we have recently postulated that diaphragm atrophy or loss of force in animal models of HFrEF depends on disease severity (3).

The systemic factors leading to diaphragm atrophy and contractile dysfunction in HFrEF appear to involve neurohumoral and inflammatory signaling (3). These signaling events culminate in accumulation of reactive oxygen species and an oxidized shift in the intracellular redox balance (14, 15). Knockout of oxidant-producing enzymes or systemic antioxidant interventions prevent diaphragm weakness in HFrEF (8, 9, 16), suggesting that oxidants alter abundance or function of proteins to cause loss of force. Oxidant-signaling activates proteolytic pathways and increases protein degradation (17). One of the main mechanisms of oxidant-mediated cellular signaling is through reversible oxidation of cysteine residues or other thiol groups in proteins (18). For instance, reversible cysteine oxidation of myofibrillar and calcium-handling proteins lowers skeletal muscle shortening and force (19–22). It is important to note, however, that the specific changes in protein abundance and thiol redox modifications of proteins associated with diaphragm abnormalities in HFrEF remain unknown.

The main goal of our study was to understand the physiological and molecular basis of diaphragm weakness in HFrEF. We tested the hypothesis that diaphragm atrophy and loss of force depend on severity of HFrEF. Overall, diaphragm abnormalities were more

pronounced in severe HFrEF. *Therefore, we performed global label free proteomics and differential cysteine labeling focused on diaphragm of rats with severe HFrEF and healthy controls to better understand the protein abundance and redox modifications associated with diaphragm weakness.* Our general hypotheses were that severe HFrEF increased proteins of catabolic pathways, decreased abundance of myofibrillar proteins, and heightened reversibly oxidized proteins in the diaphragm. Our data partially supported our hypotheses and reveal novel candidate mechanisms of diaphragm atrophy and contractile dysfunction, which include decreased abundance of key components of anabolic pathways and increased reversibly oxidized thiol groups in thin-filament proteins.

## 2. Materials and methods

### 2.1 Animals and Surgical Intervention

All procedures conformed to the guiding principles for use and care of laboratory animals of the American Physiological Society and were approved by the University of Florida Institutional Animal Care and Use Committee (IACUC 201607964). Adult male Sprague-Dawley rats (initially 8–10 weeks old) were used in the present study. Rats were housed at the University of Florida under 12h:12h light-dark cycle and had access to standard chow and water ad libitum. Rats were randomly assigned to undergo myocardial infarction (44% mortality rate; n = 14 in final experiments) or sham (n = 15) surgery.

For survival surgeries (8, 23), rats were anaesthetized using isoflurane and intubated for mechanical ventilation. We exposed the heart through a left thoracotomy and removed the pericardium to ligate the coronary artery using 6–0 monofilament absorbable suture (Demesorb; Demetech, Miami, FL, USA). To elicit a large infarct, we placed the suture under or near the edge of the left atrium to ligate the left anterior descending artery proximal to all of its branches (64% mortality, n = 5 in final experiments). To elicit small-to-medium infarcts, we placed the suture ~2–3 mm from the edge of the left atrium toward the apex of the heart to ligate the LAD and some, but not all, of its branches (31% mortality, n = 9 in final experiments). We closed the thoracic and skin incisions with 3–0 absorbable (Demesorb) and nylon sutures (Demelon), respectively. Sham operations mimicked the myocardial infarction procedure without ligation of the artery. Post-operation, animals received topical bupivacaine once and subcutaneous buprenorphine immediately and twice daily for 3 days.

### 2.2 Cardiac Function

Cardiac function was evaluated within 2–4 weeks of terminal experiments using echocardiography or cardiac magnetic resonance imaging. For echocardiography, two-dimensional M-mode ultrasound images at 7.5 MHz (Aplio, Toshiba America Medical Systems, Tustin, CA, USA) were obtained in the parasternal short-axis view. Animals were maintained at 1.5–2.5% isoflurane anesthesia and ECG electrodes were placed on the limbs to monitor heart rate. The level of anesthesia was adjusted as needed to maintain heart rate between 400–500 bpm. Image J software was used to quantify ventricle diameters from ultrasound images. In a subset of animals (n = 3 MI, 2 Sham), we assessed cardiac function via magnetic resonance imaging (MRI). Cardiac MRI was performed in a 4.7-T, horizontal

bore magnet (VMJ version 3.1; Agilent, Santa Clara, CA). Rats were anesthetized and positioned prone on a custom-built setup that allowed monitoring of body temperature, respiratory rate, and heart rate. ECG electrodes were inserted in limbs and respiration pad was taped across abdomen. Rats were maintained under anesthesia (1.5–2.5% isoflurane) via nose cone and were placed in the magnet. Average body temperature of the rat was maintained at 37°C using a circulating water heater. We adjusted the level of anesthesia to maintain heart rate as described above and respiratory rate of 50–60 breaths/minute. Rats were imaged using quadrature birdcage volume coil. A series of five transverse images were acquired over the heart after power calibration and global shimming scans. Single slice long axis axial and sagittal scans were acquired to view the apex and base of the heart. These long axis scans were used as a reference to obtain the short axis scans, which were then used to measure ventricular function. Left and right ventricles were imaged using a stack of short axis images with 1mm slice thickness. Images were acquired using a spoiled gradient-echo cine sequence (TR = 110 ms, TE = 1.37 ms, Flip angle = 15°, FOV = 25× 25 mm<sup>2</sup>, data matrix = 128×128, and 1 mm slice thickness). Twelve cine frames were acquired through the cardiac cycle and were ECG triggered to R wave with R-R delay of 110 ms and delay of 0.2 ms. We used ultrasound and magnetic resonance images to measure left ventricular internal diameter during diastole (LVIDd) and systole (LVIDs) and calculate fractional shortening (%) as (LVIDd-LVIDs)/LVIDd × 100.

### 2.3 Tissue harvesting, infarct size, and HFrEF severity distinction

Terminal experiments were conducted 16 weeks post-operation for assessment of diaphragm contractile function, fiber cross-sectional area, and proteomic profile. On the day of experiment, we anaesthetized rats using isoflurane and performed a laparotomy and thoracotomy to collect blood and tissue samples. Blood was sampled from the inferior vena cava and processed for serum (BD Vacutainer). The diaphragm was quickly excised, placed in ice cold Krebs Ringer solution (in mM: 137 NaCl, 5 KCl, 1 MgSO<sub>4</sub>, 1 NaH<sub>2</sub>PO<sub>4</sub>, 24 NaHCO<sub>3</sub>, and 2 CaCl<sub>2</sub>), and costal diaphragm was processed and allocated for contractile, histological, and biochemical assays. The heart was then excised, ventricles dissected and weighed, and left ventricle infarct size calculated using planimetry. Severe HFrEF (sHFrEF) was defined based on two criteria: 1) infarct size >35% of left ventricle and septum, and 2) right ventricle hypertrophy (i.e., RV/tibia length > 2 SDs above the sham average). These criteria have been shown to accurately predict severe heart failure as defined by standard measurements, such as invasive cardiac hemodynamics (Pfeffer et al., 1979; Fletcher et al., 1981; Nahrendorf et al., 2001; Nahrendorf et al., 2003; Finsen et al., 2005; Aronsen et al., 2017). Animals that had a transmural infarct, but did not meet both of these criteria were considered to have moderate HFrEF (mHFrEF). We also measured serum levels of brain natriuretic peptide (BNP) using an enzyme-linked immunosorbent assay (ELISA) (RayBiotech, Norcross, GA, USA, Cat # EIAR-BNP).

### 2.4 Diaphragm isometric contractile properties in vitro

A costal diaphragm bundle maintaining a segment of the rib and central tendon was dissected for attachment to a muscle mechanics apparatus (Aurora Scientific, 300C L-R model) for analysis of contractile properties as previously described (8, 23). Briefly, the bundle was placed at optimal length and kept in Krebs Ringer solution (25°C) gassed with a

mixture of 95% O<sub>2</sub> and 5% CO<sub>2</sub> throughout the procedure. We measured isometric force during twitch (1 Hz) and maximal tetanic stimulations (120 Hz) using 600 mA current and 0.25 ms pulse. *Following twitch and tetanic measurements at 25°C, we determined the isometric force-frequency relationship at 37°C* (8). To estimate the bundle cross-sectional area, diaphragm bundle weight (g) was divided by bundle length (cm) multiplied by muscle specific density (1.056 g/cm<sup>3</sup>). *We used a four-parameter Hill equation to define the shape of the force-frequency relationship* (8).

## 2.5 Fiber distribution and cross sectional area

Histological analysis for fiber distribution and cross-sectional area was conducted as detailed previously (8, 24). An isolated diaphragm bundle was embedded in Tissue-Tek OCT freezing medium, frozen in liquid-nitrogen-cooled isopentane, and stored at -80°C until cryo-sectioning. We cut 10 µm cross sections using a cryostat (Leica, CM 3050S model) cooled to approximately -20°C and then transferred sections to frosted microscope slides. Sections underwent several incubations and washes at room temperature for staining of fiber size and type. First, sections were covered with 1:200 wheat germ agglutinin (WGA) Texas Red (Molecular Probes) for 1 hour, washed in PBS (3 × 5 min), permeabilized with 0.5% Triton X-100 solution (5 min), and washed again in PBS (5 min). Afterward, slides were placed in a humid chamber for 90 min of primary antibody incubation. We used primary antibodies for myosin heavy chain (MyHC) type I (A4.840, 1:15; Developmental Studies Hybridoma Bank) and MyHC type IIa (SC-71, 1:50; Developmental Studies Hybridoma Bank). After the primary antibody incubation, sections were washed in PBS (3 × 5 min) and covered with fluorescently conjugated secondary antibodies for 60 min (Goat × Mouse IgM Alexa 350 and Goat × Mouse IgG Alexa 488, Invitrogen). Finally, sections were washed in PBS (3 × 5 min), allowed to dry, and imaged.

We acquired and merged diaphragm images using an inverted fluorescence microscope (Axio Observer, 10x objective lens) connected to a monochrome camera (Axio MRm, 1x c-mount, 2/3" sensor) and Zen Pro software (Carl Zeiss Microscopy). We used semi-automatic muscle analysis using segmentation of histology (SMASH) code, run in MATLAB software, to quantify fiber type distribution and fiber cross-sectional area for multiple images per rat (25). For each rat, we analyzed 500 to 2,075 fibers depending on size of diaphragm bundle.

## 2.6 Global and thiol redox proteomics

We froze diaphragm bundles allotted to proteomics analysis (*Sham and severe HFrEF*) in liquid nitrogen immediately upon bundle separation and removal of fat and excess connective tissue. Frozen samples were stored on dry ice or -80°C until further processing for protein extraction and cysteine labeling, LC-MS/MS, and label-free and redox MS Quantification (26). *Briefly, each muscle was immediately placed in d0 NEM blocking buffer to prevent Cys oxidation. Tissues were homogenised in ice cold buffer (25 mM Ammonium bicarbonate containing 25 mM NEM and 0.01% Rapigest (Waters, Manchester, UK) pH 8) using a hand homogenizer. Samples were passed through a Zeba desalting column 7K MWCO (Thermo Scientific, Hempstead, UK) to remove excess d0 NEM and protein concentrations were calculated using the Bradford (BioRad, Hertfordshire, UK) method using BSA as a standard. 100 µg of protein was aliquoted and reversibly oxidised*

*Cys residues were reduced using tris (2-carboxyethyl) phosphine (TCEP) at a final concentration of 10 mM, newly reduced Cys residues were subsequently labelled with d5 NEM final concentration 20 mM. Protein extracts were digested overnight at 37 °C with trypsin. Rapigest was precipitated by addition of trifluoroacetic acid (TFA) and subsequent centrifugation before analysis by MS. Proteomics was performed using an Ultimate 3000 RSLC Nano system (Thermo Scientific) coupled to a Q-Exactive mass spectrometer (Thermo Scientific) as previously described (26). Detection of the peptides was performed by data dependent acquisition (DDA) which takes a select number of peptide peaks from the initial scan according to a rule set and the corresponding ions are then verified against this initial set via tandem mass spectrometry (MS/MS). The advantage of performing global and redox proteomics simultaneously is that changes in redox peptides can be analyzed and interpreted in the context of protein abundance measured within the same run on the mass spectrometer. The mass spectrometry proteomics data have been deposited to the ProteomeXchange Consortium via the PRIDE partner repository with the dataset identifier PXD012500.*

## 2.7 Myofibrillar protein content, Oxidation, and Immunoblotting

To quantify myosin heavy chain and actin abundance, we used a tissue homogenization protocol optimized for MHC and actin solubilization (27, 28). Briefly, approximately 5 mg of diaphragm samples were glass homogenized in ice-cold high-salt lysis buffer (300 mM NaCl, 0.1 M NaH<sub>2</sub>PO<sub>4</sub>, 0.05 M Na<sub>2</sub>HPO<sub>4</sub>, 0.01 M Na<sub>4</sub>P<sub>2</sub>O<sub>7</sub>, 1 mM MgCl<sub>2</sub>, 10 mM EDTA, and 1 mM DTT, pH 6.5) and Halt protease inhibitor (Thermo Scientific). Lysates were spun at 16,000g for 3 min at 4°C and protein contents determined by Bradford assay (Bio-Rad). Samples were mixed in 2x Laemmli buffer (Bio-Rad) with DTT (0.35 M) and heat-denatured for 5 min prior to loading. We loaded ~0.4 µg protein/lane, which was within the linear range determined in our laboratory, into a 4–20% polyacrylamide gel (Criterion TGX Stain-Free Protein Gel) and performed electrophoresis at 200 V for 60 min on ice. Gels were scanned to quantify total protein and MyHC content per lane (Gel Doc EZ Imager; Bio-Rad). Densitometric analyses of MyHC bands and total protein in each lane were conducted using Image Lab 5.0 software (Bio-Rad). *We confirmed that this approach yields similar results to the Coomassie blue-based dye method of gel staining performed by our group (27). However, the stain-free gel signal has a pattern apparently inconsistent with MyHC and actin stoichiometry in skeletal muscle, which is not the case when samples are stained with a Coomassie blue-based dye (data not shown).*

Diaphragm processing for myofilament protein enrichment proceeded as described previously (29, 30), with some modifications. Briefly, diaphragm was homogenized on ice using a glass mortar and pestle with standard relaxation buffer (75 mM KCl, 10 mM imidazole pH 7.2, 2 mM MgCl<sub>2</sub>, 2 mM EDTA, 1 mM NaN<sub>3</sub>) with Triton X-100 (1:100), with Triton X-100, protease and phosphatase inhibitors (Sigma P8340 and P0044, 1:100), and N-ethylmaleimide (NEM, 1 mM) to maintain non-reducing conditions while still preventing in vitro oxidation of thiol groups (31). The ratio of tissue weight (mg) to buffer volume (µl) was 20:1 (w/v). Homogenates were then centrifuged at 16,000 g, 4°C for 1 minute. After decanting the supernatant, the pellet was re-suspended with 1 ml standard relaxation buffer with Triton X-100, vortexed, and homogenized again. Homogenates were



again spun at 16,000 g, 4°C for 1 minute. The pellet was washed in standard relaxation buffer without detergent and underwent a third spin at 16,000 g, 4°C for 1 minute. At room temperature, the pellet was vortexed and homogenized in 1:20 (w/v) 2x Laemmli buffer and then underwent twice shaking for 30 minutes and 3 seconds sonication. Samples were then spun at 18,000 g, room temperature, and the supernatant was saved for use in tropomyosin assays. Negative and positive controls for tropomyosin oxidation were sham diaphragm processed as above with the addition of 75 mM dithiothreitol (DTT) to homogenization buffer or incubation of tissue with 1 mM H<sub>2</sub>O<sub>2</sub> for 30 minutes prior to processing, respectively. Protein contents of each sample was determined via electrophoresis (200V, 65 min, 4°C) of Stain-Free gel and using albumin (P0834, Sigma-Aldrich) as protein standard.

To probe for myosin light chain (total and phospho) via immunoblotting, samples were homogenized at 4°C using stainless steel beads and bullet blender (BBY24M, Next Advance) in 1x cell lysis buffer (n°. 9803; Cell Signaling Technology) containing the following: 20 mM Tris-HCl (pH 7.4), 150 mM NaCl, 1 mM Na<sub>2</sub>EDTA, 1 mM EGTA, 1% Triton, 2.5 mM sodium pyrophosphate, 1 mM β-glycerophosphate, 1 mM Na<sub>3</sub>VO<sub>4</sub>, 1 µg/ml leupeptin, and 1x Halt protease and phosphatase inhibitors (Thermo Scientific). Bead pelleting and crude lysate clearing was achieved by centrifugation (5,000 g at 4°C for 2 min) and the initial supernatant (S1) was then rotated end-over-end for 1 hour, sonicated 2 × 3 s, and centrifuged at 15,000 g for 10 minutes at 4°C, and supernatant (S2) was saved for quantification of protein content (DC assay, Bio-Rad) and gel-loading.

After quantification of protein content in standard or myofibrillar protein-enriched preps, samples were mixed in 2x Laemmli buffer (Bio-Rad) containing DTT (0.35 M) and heat-denatured for 5 min. We loaded approximately 10–25 µg of protein per lane into a 4–20% polyacrylamide gel (Criterion TGX Stain-Free Protein Gel), and performed electrophoresis at 200 V for 60 min on ice. After electrophoresis, gels were scanned (Gel Doc EZ Imager; Bio-Rad) to image total protein per lane and signals were quantified using Image Lab 5.0 software (Bio-Rad). We then transferred the proteins to a nitrocellulose membrane overnight using 100 mA current at 4°C. After transfer, the membrane was washed for 5 min with TBS and incubated in blocking buffer (LI-COR, Lincoln, NE) at room temperature for 1 hour. After decanting blocking buffer, we incubated the membrane overnight at 4°C in primary antibody for actin (JLA-20, DSHB mouse monoclonal), total myosin light chain 2 (ALX-BC-1150-S clone F109.3E1, Enzo Life Sciences), phospho-myosin light chain (ab2480, Abcam), or tropomyosin (T9283, Sigma Aldrich) diluted 1:1000 in blocking buffer. Following primary antibody incubation, we washed the membrane 4×5 min with TBS-T, and then incubated it with secondary antibody (IR Dye, 1:20,000; LI-COR) at room temperature for 1 hour. Finally, after 4×5 min washes with TBS-T and 1×5 min wash with TBS, the membrane was scanned using an Odyssey Infrared Imaging system (LI-COR, Lincoln, NE). We quantified the immunoblot signal using Image Studio Lite (LI-COR). Gel Band Fitter Software (32) differentiated the signal for each tropomyosin isoform in the oxidized band. The immunoblot signal of each target protein was normalized to the total protein signal measured in the corresponding lanes.

We used pooled samples to test the linear range for all proteins and post-translational modifications measured in our study and loaded protein contents that were approximately in

the mid-portion of the linear relationship for each target protein. Each gel/membrane also included an abbreviated (at least 3 points) linearity test with pooled samples to confirm that individual samples were loaded within the linear range of the assay and normalize the signal to total protein in each lane. All data reported herein are from samples within the linear range of measurement for target and reference protein(s).

## 2.8 Statistical analysis

We compared groups using parametric or non-parametric ANOVA as well as Student's t-test when comparing only 2 groups (Prism 6, GraphPad Software Inc., La Jolla, CA). Parametric and non-parametric tests were used based on results from normality and equal variance tests (Sigma Plot v.13, Systat). Fiber type cross-sectional area data for 3 groups were analyzed using a linear mixed model (R Core Team, 2017) due to a different number of fibers being measured per animal. All measured fiber cross-sectional areas were inputted into 6 independent mixed effects models by fiber type (i.e., type I, type IIa, or type IIb/x) and comparison (mHFrEF vs Sham and sHFrEF vs Sham). These models assumed homogenous variance of fiber size within each fiber type. Animal group (Sham, mHFrEF, or sHFrEF) was entered as fixed effect and the interaction of animal group and animal identification number were random effects. All data are shown as mean  $\pm$  SD or scatter plots with bars indicating group mean.

We performed global quantification of proteins using PEAKS software. *We considered statistically significant changes in protein abundance when ANOVA p-value < 0.05 (calculated using label-free Top3 method contained within Peaks software), fold change 1.5, each protein with at least three unique peptides, and a false discovery rate (FDR) of 1% (26). The FDR, in this case, refers to the confidence of protein identification. We opted for using a cutoff in fold change and multiple unique peptides to diminish the FDR of significantly changed proteins and strengthen our analysis over a posthoc test with FDR-adjusted p-values. Our rationale was that the criteria using p-values adjusted based on FDR of multiple comparison could mask 'true positives' in our analysis with n = 5/group (33).*

PEAKS software also includes a post-translational modification (PTM) algorithm, where PTMs are assessed under the same criteria as for protein abundance. *Cys containing peptides that were identified with high confidence as labelled with both the d(0) and d(5) NEM (individual peptide Mascot score > 20) were considered redox peptides. We conducted a targeted post search analysis of differentially labeled Cys residues using Skyline (34) to relatively quantify the ratio of the Cys containing peptides labelled with both "light" d(0) NEM for reduced Cys residues and "heavy" d(5) NEM for reversibly oxidized Cys residues. Methionine oxidation was included as a default in database searching, but we analyzed it further because previous studies have shown that methionine oxidation impairs function in sarcomeric proteins. We determined the sum of the area of precursor ion, precursor + M1, and precursor + M2 from peptides of sarcomeric proteins containing a single oxidized methionine residue. We also normalized the oxidized methionine area to the specific protein abundance obtained from PEAKS software.*

In general, we used the conventional p-value of less than 0.05 to declare statistical significance, but wherever feasible we report exact p-values for each comparison. According



to recent recommendations (35), it is important to interpret p-values carefully, considering the number of samples and variability within the data in each comparison.

### 3. Results

#### 3.1 Animals

The characteristics of Sham, mHFrEF, and sHFrEF rats used for measurements of diaphragm isometric function, fiber cross-sectional area, and proteomic analysis are shown in Table 1. Rats with mHFrEF and sHFrEF demonstrated reduced fractional shortening, which is a defining characteristic of HFrEF. As expected by design, infarcted area of the left ventricle and right ventricle hypertrophy were higher in sHFrEF compared to mHFrEF. Serum BNP, a biomarker of heart failure, was significantly elevated when all HFrEF animals were compared to sham ( $p = 0.016$ ). Nine out of eleven animals in the HFrEF group had a BNP mean + 2 standard deviations of the Sham. However, variability in the data prevented detection of potential statistically significant differences between mHFrEF vs Sham or mHFrEF vs sHFrEF groups.

#### 3.2 Diaphragm contractile function and fiber cross-sectional area

A comparison of Sham ( $n = 10$ ) vs. all HFrEF animals ( $n = 11$ ) showed decreased maximal specific force (in  $\text{N}/\text{cm}^2$ :  $27 \pm 1.1$  and  $23 \pm 3.1$ ,  $p = 0.006$  by t-test), but no statistically significant difference in twitch specific force (in  $\text{N}/\text{cm}^2$ :  $10.7 \pm 1.8$  and  $9.4 \pm 2.1$ ,  $p = 0.13$  by t-test). Disease severity differentially influenced HFrEF's effect on diaphragm isometric contractile properties. In mHFrEF, twitch and maximal specific force showed no statistically significant difference from Sham, whereas sHFrEF animals demonstrated lower diaphragm twitch and maximal specific force than Sham and mHFrEF (Figure 1A–B). Disease severity had no effect on time-to-peak tension (in ms: Sham  $50.5 \pm 5$ , mHFrEF  $53 \pm 2$ , sHFrEF  $51 \pm 3$ ,  $p = 0.594$ ) or 1/2 relaxation time (in ms: Sham  $57 \pm 11$ , mHFrEF  $60 \pm 9$ , sHFrEF  $55 \pm 7$ ,  $p = 0.746$ ). *HFrEF also had no effect on twitch-to-tetanus ratio (Sham  $0.40 \pm 0.06$ , mHFrEF  $0.43 \pm 0.06$ , sHFrEF  $0.36 \pm 0.05$ ,  $p > .197$ ). For measurements at  $37^\circ\text{C}$ , twitch and tetanic forces were consistent with the results reported above and there was no shift in the force-frequency relationship (Supplemental Results, Figure 1).*

Immunohistochemistry analysis of diaphragm bundles from sham ( $n = 10$ ) and all HFrEF animals combined ( $n = 10$ ) showed decreased cross sectional area (in  $\mu\text{m}^2$ ) for fiber type IIb/x (Sham  $7,216 \pm 1,872$ , HFrEF  $5,215 \pm 1,369$ ;  $p = 0.013$ ), type IIa (Sham  $2,713 \pm 675$ , HFrEF  $2,194 \pm 315$ ;  $p = 0.041$ ), and type I (Sham  $2,256 \pm 484$ , HFrEF  $1,899 \pm 256$ ;  $p = 0.053$ ). The decrease in fiber cross-sectional area was independent of disease severity (Figure 1C–D). Linear mixed model analyses similarly showed that type IIb/x fibers decreased in size (~30% lower CSA) in both mHFrEF and sHFrEF compared to Sham. Type IIa fibers showed a trend toward smaller CSA in mHFrEF and sHFrEF. Type I fibers did not reach the threshold for statistical significance in mHFrEF and sHFrEF compared to Sham. The percentage distribution of type I (Sham  $40 \pm 4$ , mHFrEF  $38 \pm 3$ , and sHFrEF  $40 \pm 9$ ), type IIa (Sham  $34 \pm 3$ , mHFrEF  $35 \pm 4$ , and sHFrEF  $37 \pm 3$ ), and type IIb/x (Sham  $26 \pm 5$ , mHFrEF  $27 \pm 5$ , and sHFrEF  $21 \pm 3$ ) fibers was not different among groups.

### 3.3 Label-free proteomic analysis of diaphragm muscle from sham and severe HFrEF rats

There were 873 proteins detected in all samples with shotgun proteomics, with 35 being upregulated and 63 being downregulated 1.5 fold in sHFrEF. Of these, 5 (upregulated and all sarcomeric proteins) and 9 (downregulated) proteins met the criteria of at least 3 unique peptides/protein and  $p < 0.05$  as shown in the heat-map and volcano plot (Figure 2). Supplemental Methods *as well as* Supplemental Results (Spreadsheets 1 and 2) contain a summary of the data analysis, a list of all identified and quantified proteins, and a list of significantly changed proteins, respectively. StringDB analysis of proteins with average change 1.5 fold revealed functional enrichments in several Gene Ontology networks (e.g., cytoskeleton, actin filament binding, and mesenchyme migration) and Reactome Pathways (striated muscle contraction) (Supplemental Results, Table 1). Analysis of proteins with average change 1.5 fold revealed enrichments in Gene Ontology networks (e.g., translation, ribosome, and RNA binding) and Reactome Pathways (e.g., glycolysis and metabolism of carbohydrates) (Supplemental Results, Table 2).

Based on our label-free proteomics findings there was an increase in actin  $\alpha$  skeletal muscle, myosin's 3 and 8, tropomyosin, and  $\alpha$ -actinin in response to sHFrEF. We also measured MHC (gel electrophoresis) and actin abundance (immunoblotting) and found no statistically significant difference between Sham and sHFrEF (Figure 3A–B). A specific finding from proteomics potentially relevant to muscle contractile function was decreased myosin light chain kinase 2 in sHFrEF. This led us to determine the phosphorylation status of regulatory MLC. Immunoblots showed no statistically significant difference between Sham and HFrEF for regulatory MLC phosphorylation (Figure 3C–D) or abundance (data not shown).

### 3.4 Redox status of proteins in diaphragm of sham and sHFrEF rats

We completed targeted analysis of peptides identified from fragmentation of parent ions with light and heavy NEM to calculate the ratio intensity of reduced/reversibly oxidized Cys residues, which indicates a predominantly reduced state (ratio  $> 1.0$ ) or oxidized state (ratio  $< 1.0$ ). Figure 4A and Table 2 show the redox state of specific cysteine residues identified in myofilament and structural proteins. In most of these proteins, sHFrEF caused a shift towards greater Cys oxidation, represented by a decrease in the reduced/reversibly oxidized ratio. Filamin C, a Z-line protein, had the residue (Cys2661) with largest increase in oxidation for sHFrEF vs. Sham. Of particular interest for contractile function, sHFrEF caused a significant shift to a more oxidized state in slow- (Cys29) and fast-TnI (Cys134), and  $\beta$ -tropomyosin (Cys190). Oxidation of Tm Cys190 results in formation of Tm dimers via disulfide bond that can be detected via non-reducing gel electrophoresis (31, 36). Non-reducing gel electrophoresis and immunoblot confirmed heightened oxidation of  $\beta$ -Tm and no statistically significant difference in  $\alpha$ -Tm oxidation in sHFrEF vs. Sham (Figure 4B–C).

Figure 4D–E and Table 3 show redox state of cysteine residues from other proteins (e.g., cytosolic, mitochondrial) with  $p$ -value less than 0.05 for comparison between Sham and sHFrEF. Proteins involved in metabolism and calcium handling showed a shift toward greater oxidation of Cys residues in sHFrEF (e.g. pyruvate kinase; SERCA pump, fast isoform). Cysteine residues from proteins involved in cell signaling (e.g., protein phosphatase 2A catalytic subunit) shifted toward a more reduced state in sHFrEF.

Our analysis also revealed increases in oxidized methionine residues in skeletal muscle  $\alpha$ -actin and Myl1. Oxidized actin methionine residues 46, 192, 301, and 308 were increased to 1.5- to 4-fold in sHFrEF samples compared to Sham, with Met46 and Met301 reaching the  $p < 0.05$  criteria (Figure 5A). When normalized to total actin abundance, oxidized Met46 and Met301 in sHFrEF were increased to 2-fold relative to Sham (Figure 5B). Regarding Myl1, the level of oxidized Met98 was elevated when analyzed in absolute area (relative to Sham average: Sham  $1.0 \pm 0.66$ , sHFrEF  $2.23 \pm 0.56$ ;  $p = 0.013$ ), but not after normalization to total Myl1 abundance (Sham  $1.0 \pm 0.95$ , sHFrEF  $1.38 \pm 0.39$ ;  $p = 0.39$ ).

## 4. Discussion

The main findings of our study were: 1) moderate and severe HFrEF caused diaphragm fiber atrophy; 2) maximal diaphragm specific force was diminished in severe HFrEF, but not moderate HFrEF; 3) severe HFrEF decreased abundance of proteins involved in ribosomal function and glucose and glycolytic metabolism; 4) redox proteomics in severe HFrEF showed heightened reversible cysteine oxidation of thin-filament proteins, filamin C, and SERCA1, and increased methionine oxidation in sarcomeric actin. *Previous work frames diaphragm dysfunction as a significant contributor to morbidity and mortality in HFrEF patients (3–5). Thus, our results advance the field by recapitulating the progressive diaphragm pathology seen with increasing HFrEF severity and then linking this phenomenon to targetable cellular mechanisms involving protein expression and oxidation.*

### 4.1 Classification of disease severity

Based on assessment of cardiac function and severity of symptoms, patients are most commonly classified into groups that range from class I (no physical limitation during regular activities) to class IV (unable to carry on any physical activity without discomfort and dyspnea – HF symptoms at rest) using New York Heart Association criteria. Patients with severe HFrEF (Class III or IV) generate lower inspiratory pressures than patients with moderate HFrEF (Class I or II) in studies using volitional tests or phrenic nerve stimulation (13, 37). The widely used classification of HFrEF based on NYHA criteria, which relies partially on patient symptoms, cannot be replicated in rodents. Hence, we used left ventricle infarct area  $\geq 35\%$  and right ventricle hypertrophy to classify our MI animals into moderate and severe HFrEF groups. Earlier studies have shown that infarct sizes  $\geq 35\text{--}45\%$  of the left ventricle, measured by circumference, lead to severe heart failure in rats (38–41). Infarct size measured by circumference is linearly related to infarct area with a 10% offset, i.e., when infarct size by circumference is 45%, then infarct area = 35% (42). Therefore, our criterion based on the extent of infarct was on the upper end of the cutoff range reported to cause severe HFrEF.

Severe HFrEF is marked by pronounced depression of left ventricular contractility, with elevations in left ventricular end-diastolic pressure and right ventricular systolic pressure (40, 41). In its most advanced (and untreated) form, heart failure causes pulmonary arterial hypertension and lung congestion (40, 43, 44), which correlate with exercise intolerance (45), decreased maximal inspiratory pressure (13), and poor prognosis in patients (46). The consequence of pulmonary arterial hypertension and lung congestion is right ventricle

hypertrophy (47). A recent study has shown that right ventricle mass is a robust marker of severe heart failure in rats (43). Overall, these observations support our use of right ventricle hypertrophy as a criterion to classify rats with severe HFrEF.

## 4.2 Impact of disease severity on diaphragm and mechanistic insights from proteomics

In general, studies in patients with HFrEF show a decrease in maximal inspiratory pressure, and the magnitude of this decrease is associated with disease severity determined by NYHA class (3, 13, 48). This progressive pattern is seen with both voluntary efforts as well as phrenic nerve stimulation (13, 37, 49). Our data are clinically relevant because they suggest that diaphragm fiber atrophy in mHFrEF and sHFrEF, and diaphragm contractile dysfunction (defined by loss of force normalized to cross sectional area) in sHFrEF, contribute to the differential decline in inspiratory function with advancing NYHA class.

Diaphragm fiber atrophy has been a contradictory finding in HFrEF. Some studies have reported no atrophy (7, 8, 50), whereas others found atrophy ranging from 15% to 40% lower fiber cross-sectional area in HFrEF (11, 12, 51, 52). In patients with end-stage HFrEF, diaphragm fiber diameter is preserved suggesting normal cross-sectional area (53). These contradictory findings are difficult to reconcile, as there is not a consistent pattern among studies showing atrophy or lack thereof. However, two interesting aspects to consider from our current findings are: first, the presence of atrophy without statistically significant contractile dysfunction in moderate HFrEF and second, the absence of diaphragm fiber hypertrophy in rats with severe HFrEF, *where lowered respiratory system compliance* (54, 55) *and elevated ventilation* (56) *increase work of breathing*. One possibility is that a threshold of inflammatory or neurohumoral signaling may have been met to induce atrophy, but not to elicit contractile dysfunction in moderate HFrEF. Indeed, plasma data from patients have demonstrated associations between severity or functional class and progressive inflammation (57–59). Importantly, TNF- $\alpha$ , a cytokine upregulated in severe HFrEF, has been linked to contractile dysfunction (60). In severe HFrEF, we have postulated that anabolic resistance may explain absence of diaphragm hypertrophy despite elevated work of breathing (3). Anabolic resistance in aging is associated with diminished ribosome biogenesis (61, 62). Interestingly, our proteomic analysis revealed downregulation of several ribosomal proteins and, accordingly, ‘Ribosome’ emerged as an enriched functional biological network in gene ontology and KEGG pathways from our analysis of String DB. These findings prompt the speculation that therapeutic increase in ribosome biogenesis would normalize diaphragm fiber size (or promote hypertrophy) and improve inspiratory function in HFrEF.

Diaphragm contractile dysfunction is widely documented in severe HFrEF (7–10, 23, 51). However, the molecular mechanisms of diaphragm contractile dysfunction in severe HFrEF remain unclear. *HFrEF lowers calcium sensitivity and maximal calcium-activated isometric force in triton-permeabilized diaphragm fibers* (7), *where membrane depolarization and sarcoplasmic reticulum calcium release/reuptake are not involved*. These findings indicate that structural and sarcomeric protein abnormalities are important determinants of diaphragm weakness in HFrEF. Previous studies have implicated increased proteolysis and selective degradation of MHC in diaphragm weakness in HFrEF (7, 63). In contrast, our

proteomics data showed upregulation of clusters of proteins involved in striated muscle contraction, including some isoforms of MHC. However, we acknowledge that the lysis buffer used for proteomics (regular, 'low-salt') is not ideal for isolation of contractile proteins from skeletal muscle. Therefore, we further examined MHC abundance using high-salt buffer and gel-staining for MHC, which is the optimal approach for quantification of thick filament proteins (28). Following this protocol, we found no statistically significant difference between sham and sHFrEF (Figure 3A–B). Given these results, we hypothesize that atrophy resulted from homogenous loss of protein. Using this specific technique in cancer cachexia, we have previously displayed atrophy in the context of selective loss of myosin heavy chain (27) – while others have demonstrated atrophy without selective contractile protein degradation (28). It is also possible that lack of isoform specificity in our gel-based approach masked isoform-specific differences between groups. Nonetheless, the global proteomics results showed down regulation of myosin light chain kinase (Figure 2A, accession G3V731), which phosphorylates myosin regulatory light chain (64). Myosin regulatory light chain phosphorylation increases the number of cross-bridges in the disordered relaxed state (available for actin binding) and enhances contractile function (65, 66). However, we found no statistically significant difference between groups on phosphorylation status of myosin regulatory light chain (Figure 3C–D), refuting the notion that this post-translational modification underlies the contractile dysfunction in sHFrEF. Overall, our results suggest that decreased overall abundance of thin- and thick-filament proteins was not responsible for loss of diaphragm force in rats with sHFrEF in our study.

Several studies have attributed diaphragm weakness in HFrEF to impairments in redox homeostasis and protein oxidation (8–10). Exposure of muscle fibers to thiol-oxidizing agents and oxidative conditions decrease maximal force, shortening velocity, calcium sensitivity, calcium release/reuptake, and cooperativity (21, 22, 67). Mitochondria and NADPH oxidase are important sources of excess oxidants that contribute to diaphragm weakness in HFrEF (3). However, the exact molecular mechanism of contractile dysfunction caused by oxidants in HFrEF remains unclear. Oxidation of cysteine residues in sarcomeric proteins, RyR calcium channel, and SERCA impair protein function and have the potential to cause weakness (19, 20, 22). Our investigation of redox proteomics revealed, among sarcomeric proteins, reversible oxidation of cysteine residues in thin-filament proteins (troponin I, tropomyosin, and actin). Specifically, HFrEF increased reversible oxidation of fast troponin I Cys134, which modulates contractile function: S-nitrosylation diminishes calcium sensitivity, whereas S-glutathionylation transiently increases calcium sensitivity and decreases cooperativity (20, 68). However, prolonged S-glutathionylation of muscle fibers decreases calcium sensitivity and cooperativity (69). HFrEF also heightened reversible oxidation of fast tropomyosin Cys190. Tropomyosin consists of two alpha-helical polypeptide chains arranged in a coiled coil (70, 71). In this arrangement, cysteines 190 of each chain are closely juxtaposed and form a disulfide bridge under conditions of elevated oxidation (36, 70). Oxidation of Cys190 partially unfolds the alpha-helical chain, decreases tropomyosin binding to actin, and lowers actomyosin ATPase activity (36, 70, 72). Actin (Cys219) and slow TnI (Cys29) also showed a trend toward heightened reversible oxidation in sHFrEF. However, the functional effect of oxidation in these residues is unknown. Overall, heightened oxidation of cysteine residues from troponin I and tropomyosin might

contribute to the diminished calcium sensitivity that has been reported using triton-permeabilized diaphragm fibers from rats with HFrEF showing characteristics similar to severe HFrEF rats in our current study (7).

In addition to cysteine, oxidation of methionine in calcium regulatory and myofibrillar proteins impairs protein structure and function (73–75). We found that sHFrEF increased methionine oxidation of skeletal muscle  $\alpha$ -actin (Met 46/49, 192 and 301). Irradiation, which acutely shifts the cellular redox balance toward a more oxidized state, also increases oxidation of methionine residues in skeletal muscle actin (76). Actin methionine oxidation lowers protein stability, depolymerizes filamentous actin, and decreases actomyosin ATPase activity (73, 77). Interestingly, essential myosin light chains Myl1 (Met98) and Myl3 (Met57 and 70), respectively fast and slow isoforms, also emerged with heightened methionine oxidation in sHFrEF. The consequences of methionine oxidation in myosin light chains are unknown, but it has been reported under *in vitro* oxidizing conditions that impair contractile function (74). It is worth noting that oxidation of methionine residues, like other oxidative modifications, can be an artefact of sample preparation. We cannot exclude the impact of artificial oxidation during sample preparation on our results, even though we homogenized the tissue in the presence of a blocking buffer and limited exposure to air. However, all samples were prepared in the same manner and results for methionine oxidation reported herein focus on those that displayed a consistent difference between groups. It is worth noting that, with our approach, it might be only the relatively high abundant residues that we are detecting. A thorough investigation of methionine oxidation would require a dedicated approach to target this modification. Currently, our novel findings point to oxidation of methionine in skeletal muscle  $\alpha$ -actin as a potential molecular modification underlying diaphragm contractile dysfunction in sHFrEF.

## 5. Summary and conclusions

Our study shows that diaphragm fiber atrophy occurs in moderate and severe HFrEF, and loss of diaphragm fiber force occurs in severe HFrEF. These factors are the most likely culprits in the progressive decline in inspiratory function in patients. Our global proteomic analysis revealed downregulation of ribosomal and glucose metabolism/glycolysis proteins that will contribute to fiber atrophy or anabolic resistance and further accelerate fatigue in severe HFrEF. The redox proteomics investigation showed, among sarcomeric proteins, heightened abundance of reversibly oxidized cysteine and methionine residues in thin-filament proteins (troponin I, tropomyosin, and actin). These redox modifications are known to decrease skeletal muscle calcium sensitivity, shortening velocity, and force – contractile abnormalities previously reported in severe HFrEF. Overall, our data outline intrinsic abnormalities in diaphragm morphology, contractile function, metabolism, and redox balance as therapeutic targets to prevent or mitigate the progressive inspiratory impairment in HFrEF.

## Supplementary Material

Refer to Web version on PubMed Central for supplementary material.



## Acknowledgements

We would like to thank Philip Coblentz, Nikhil Patel, and Ravi Patel for technical assistance. A portion of this work was performed in the McKnight Brain Institute at the National High Magnetic Field Laboratory's AMRIS Facility, which is supported by National Science Foundation Cooperative Agreement No. DMR-1644779\* and the State of Florida.

### Funding

This study was funded by NIH grants R01 HL130318-01 (L.F. Ferreira) and BREATHE T32 HL134621 (trainee: R.C. Kelley, principal investigator: Gordon S. Mitchell, University of Florida).

## References

1. Mantilla CB, Seven YB, Zhan WZ, Sieck GC. Diaphragm motor unit recruitment in rats. *Respir Physiol Neurobiol.* 2010;173(1):101–6. [PubMed: 20620243]
2. Cahalin LP, Arena R, Guazzi M, Myers J, Cipriano G, Chiappa G, et al. Inspiratory muscle training in heart disease and heart failure: a review of the literature with a focus on method of training and outcomes. *Expert Rev Cardiovasc Ther.* 2013;11(2):161–77. [PubMed: 23405838]
3. Kelley RC, Ferreira LF. Diaphragm abnormalities in heart failure and aging: mechanisms and integration of cardiovascular and respiratory pathophysiology. *Heart Fail Rev.* 2017;22(2):191–207. [PubMed: 27000754]
4. Meyer FJ, Borst MM, Zugck C, Kirschke A, Schellberg D, Kubler W, et al. Respiratory muscle dysfunction in congestive heart failure: clinical correlation and prognostic significance. *Circulation.* 2001;103(17):2153–8. [PubMed: 11331255]
5. Ramalho SHR, Cipriano Junior G, Vieira PJC, Nakano EY, Winkelmann ER, Callegaro CC, et al. Inspiratory muscle strength and six-minute walking distance in heart failure: Prognostic utility in a 10 years follow up cohort study. *PLoS One.* 2019;14(8):e0220638. [PubMed: 31369636]
6. Hamazaki N, Masuda T, Kamiya K, Matsuzawa R, Nozaki K, Maekawa E, et al. Respiratory muscle weakness increases dead-space ventilation ratio aggravating ventilation-perfusion mismatch during exercise in patients with chronic heart failure. *Respirology.* 2019;24(2):154–61. [PubMed: 30426601]
7. van Hees HW, van der Heijden HF, Ottenheijm CA, Heunks LM, Pigmans CJ, Verheugt FW, et al. Diaphragm single-fiber weakness and loss of myosin in congestive heart failure rats. *Am J Physiol Heart Circ Physiol.* 2007;293(1):H819–28. [PubMed: 17449557]
8. Laitano O, Ahn B, Patel N, Coblentz PD, Smuder AJ, Yoo JK, et al. Pharmacological targeting of mitochondrial reactive oxygen species counteracts diaphragm weakness in chronic heart failure. *J Appl Physiol (1985).* 2016;120(7):733–42. [PubMed: 26846552]
9. Ahn B, Beharry AW, Frye GS, Judge AR, Ferreira LF. NAD(P)H oxidase subunit p47phox is elevated, and p47phox knockout prevents diaphragm contractile dysfunction in heart failure. *Am J Physiol Lung Cell Mol Physiol.* 2015;309(5):L497–505. [PubMed: 26209274]
10. Mangner N, Bowen TS, Werner S, Fischer T, Kullnick Y, Oberbach A, et al. Exercise Training Prevents Diaphragm Contractile Dysfunction in Heart Failure. *Med Sci Sports Exerc.* 2016;48(11):2118–24. [PubMed: 27327028]
11. Stassijns G, Gayan-Ramirez G, De Leyn P, Verhoeven G, Herijgers P, de Bock V, et al. Systolic ventricular dysfunction causes selective diaphragm atrophy in rats. *Am J Respir Crit Care Med.* 1998;158(6):1963–7. [PubMed: 9847293]
12. Gillis TE, Klaiman JM, Foster A, Platt MJ, Huber JS, Corso MY, et al. Dissecting the role of the myofilament in diaphragm dysfunction during the development of heart failure in mice. *Am J Physiol Heart Circ Physiol.* 2016;310(5):H572–86. [PubMed: 26702144]
13. Filusch A, Ewert R, Altesellmeier M, Zugck C, Hetzer R, Borst MM, et al. Respiratory muscle dysfunction in congestive heart failure--the role of pulmonary hypertension. *Int J Cardiol.* 2011;150(2):182–5. [PubMed: 20444510]
14. Dikalov S Cross talk between mitochondria and NADPH oxidases. *Free Radic Biol Med.* 2011;51(7):1289–301. [PubMed: 21777669]

15. Supinski GS, Alimov AP, Wang L, Song XH, Callahan LA. Neutral sphingomyelinase 2 is required for cytokine-induced skeletal muscle calpain activation. *Am J Physiol Lung Cell Mol Physiol*. 2015;309(6):L614–24. [PubMed: 26138644]
16. Supinski GS, Callahan LA. Diaphragmatic free radical generation increases in an animal model of heart failure. *J Appl Physiol*. 2005;99(3):1078–84. [PubMed: 16103520]
17. Reid MB, Li YP. Cytokines and oxidative signalling in skeletal muscle. *Acta Physiol Scand*. 2001;171(3):225–32. [PubMed: 11412134]
18. Forman HJ, Fukuto JM, Torres M. Redox signaling: thiol chemistry defines which reactive oxygen and nitrogen species can act as second messengers. *Am J Physiol Cell Physiol*. 2004;287(2):C246–56. [PubMed: 15238356]
19. Andersson DC, Betzenhauser MJ, Reiken S, Meli AC, Umanskaya A, Xie W, et al. Ryanodine receptor oxidation causes intracellular calcium leak and muscle weakness in aging. *Cell Metab*. 2011;14(2):196–207. [PubMed: 21803290]
20. Dutka TL, Mollica JP, Posterino GS, Lamb GD. Modulation of contractile apparatus Ca<sup>2+</sup> sensitivity and disruption of excitation-contraction coupling by S-nitrosoglutathione in rat muscle fibres. *J Physiol*. 2011;589(Pt 9):2181–96. [PubMed: 21115647]
21. Andrade FH, Reid MB, Westerblad H. Contractile response of skeletal muscle to low peroxide concentrations: myofibrillar calcium sensitivity as a likely target for redox-modulation. *FASEB J*. 2001;15(2):309–11. [PubMed: 11156946]
22. Posterino GS, Lamb GD. Effects of reducing agents and oxidants on excitation-contraction coupling in skeletal muscle fibres of rat and toad. *J Physiol*. 1996;496 ( Pt 3):809–25. [PubMed: 8930846]
23. Empinado HM, Deevska GM, Nikolova-Karakashian M, Yoo JK, Christou DD, Ferreira LF. Diaphragm dysfunction in heart failure is accompanied by increases in neutral sphingomyelinase activity and ceramide content. *Eur J Heart Fail*. 2014;16(5):519–25. [PubMed: 24596158]
24. Kelley RC, McDonagh B, Ferreira LF. Advanced aging causes diaphragm functional abnormalities, global proteome remodeling, and loss of mitochondrial cysteine redox flexibility in mice. *Exp Gerontol*. 2018;103:69–79. [PubMed: 29289553]
25. Smith LR, Barton ER. SMASH - semi-automatic muscle analysis using segmentation of histology: a MATLAB application. *Skelet Muscle*. 2014;4:21. [PubMed: 25937889]
26. McDonagh B, Sakellariou GK, Smith NT, Brownridge P, Jackson MJ. Differential cysteine labeling and global label-free proteomics reveals an altered metabolic state in skeletal muscle aging. *J Proteome Res*. 2014;13(11):5008–21. [PubMed: 25181601]
27. Roberts BM, Ahn B, Smuder AJ, Al-Rajhi M, Gill LC, Beharry AW, et al. Diaphragm and ventilatory dysfunction during cancer cachexia. *FASEB J*. 2013;27(7):2600–10. [PubMed: 23515443]
28. Cospier PF, Leinwand LA. Myosin heavy chain is not selectively decreased in murine cancer cachexia. *Int J Cancer*. 2012;130(11):2722–7. [PubMed: 21796617]
29. Solaro RJ, Pang DC, Briggs FN. The purification of cardiac myofibrils with Triton X-100. *Biochim Biophys Acta*. 1971;245(1):259–62. [PubMed: 4332100]
30. Scruggs SB, Reisdorph R, Armstrong ML, Warren CM, Reisdorph N, Solaro RJ, et al. A novel, in-solution separation of endogenous cardiac sarcomeric proteins and identification of distinct charged variants of regulatory light chain. *Mol Cell Proteomics*. 2010;9(9):1804–18. [PubMed: 20445002]
31. Canton M, Skyschally A, Menabo R, Boengler K, Gres P, Schulz R, et al. Oxidative modification of tropomyosin and myocardial dysfunction following coronary microembolization. *Eur Heart J*. 2006;27(7):875–81. [PubMed: 16434410]
32. Mitov MI, Greaser ML, Campbell KS. GelBandFitter--a computer program for analysis of closely spaced electrophoretic and immunoblotted bands. *Electrophoresis*. 2009;30(5):848–51. [PubMed: 19197901]
33. Pascovici D, Handler DC, Wu JX, Haynes PA. Multiple testing corrections in quantitative proteomics: A useful but blunt tool. *Proteomics*. 2016;16(18):2448–53. [PubMed: 27461997]
34. Schilling B, Rardin MJ, MacLean BX, Zawadzka AM, Frewen BE, Cusack MP, et al. Platform-independent and label-free quantitation of proteomic data using MS1 extracted ion chromatograms

in skyline: application to protein acetylation and phosphorylation. *Mol Cell Proteomics*. 2012;11(5):202–14. [PubMed: 22454539]

35. Amrhein V, Greenland S, McShane B. Scientists rise up against statistical significance. *Nature*. 2019;567(7748):305–7. [PubMed: 30894741]
36. Williams DL Jr., Swenson CA. Disulfide bridges in tropomyosin. Effect on ATPase activity of actomyosin. *Eur J Biochem*. 1982;127(3):495–9. [PubMed: 6217068]
37. Hughes PD, Polkey MI, Harrus ML, Coats AJ, Moxham J, Green M. Diaphragm strength in chronic heart failure. *Am J Respir Crit Care Med*. 1999;160(2):529–34. [PubMed: 10430724]
38. Nahrendorf M, Wiesmann F, Hiller KH, Hu K, Waller C, Ruff J, et al. Serial cine-magnetic resonance imaging of left ventricular remodeling after myocardial infarction in rats. *J Magn Reson Imaging*. 2001;14(5):547–55. [PubMed: 11747006]
39. Nahrendorf M, Hu K, Fraccarollo D, Hiller KH, Haase A, Bauer WR, et al. Time course of right ventricular remodeling in rats with experimental myocardial infarction. *Am J Physiol Heart Circ Physiol*. 2003;284(1):H241–8. [PubMed: 12388245]
40. Pfeffer MA, Pfeffer JM, Fishbein MC, Fletcher PJ, Spadaro J, Kloner RA, et al. Myocardial infarct size and ventricular function in rats. *Circ Res*. 1979;44(4):503–12. [PubMed: 428047]
41. Fletcher PJ, Pfeffer JM, Pfeffer MA, Braunwald E. Left ventricular diastolic pressure-volume relations in rats with healed myocardial infarction. Effects on systolic function. *Circ Res*. 1981;49(3):618–26. [PubMed: 7261261]
42. Finsen AV, Christensen G, Sjaastad I. Echocardiographic parameters discriminating myocardial infarction with pulmonary congestion from myocardial infarction without congestion in the mouse. *J Appl Physiol* (1985). 2005;98(2):680–9. [PubMed: 15475595]
43. Aronsen JM, Espe EKS, Skardal K, Hasic A, Zhang L, Sjaastad I. Noninvasive stratification of postinfarction rats based on the degree of cardiac dysfunction using magnetic resonance imaging and echocardiography. *Am J Physiol Heart Circ Physiol*. 2017;312(5):H932–H42. [PubMed: 28188213]
44. Philip JL, Murphy TM, Schreier DA, Stevens S, Tabima DM, Albrecht M, et al. Pulmonary vascular mechanical consequences of ischemic heart failure and implications for right ventricular function. *Am J Physiol Heart Circ Physiol*. 2019;316(5):H1167–H77. [PubMed: 30767670]
45. Butler JE, McKenzie DK, Gandevia SC. Discharge properties and recruitment of human diaphragmatic motor units during voluntary inspiratory tasks. *J Physiol*. 1999;518 ( Pt 3):907–20. [PubMed: 10420024]
46. Ghio S, Gavazzi A, Campana C, Inserra C, Klersy C, Sebastiani R, et al. Independent and additive prognostic value of right ventricular systolic function and pulmonary artery pressure in patients with chronic heart failure. *J Am Coll Cardiol*. 2001;37(1):183–8. [PubMed: 11153735]
47. Omura J, Bonnet S, Kutty S. Right ventricular and pulmonary vascular changes in pulmonary hypertension associated with left heart disease. *Am J Physiol Heart Circ Physiol*. 2019;316(5):H1144–H5. [PubMed: 30875257]
48. Kasahara Y, Izawa KP, Watanabe S, Osada N, Omiya K. The Relation of Respiratory Muscle Strength to Disease Severity and Abnormal Ventilation During Exercise in Chronic Heart Failure Patients. *Res Cardiovasc Med*. 2015;4(4):e28944. [PubMed: 26528451]
49. Howell S, Maarek JM, Fournier M, Sullivan K, Zhan WZ, Sieck GC. Congestive heart failure: differential adaptation of the diaphragm and latissimus dorsi. *J Appl Physiol* (1985). 1995;79(2):389–97. [PubMed: 7592193]
50. Lima AR, Martinez PF, Damatto RL, Cezar MD, Guizoni DM, Bonomo C, et al. Heart failure-induced diaphragm myopathy. *Cell Physiol Biochem*. 2014;34(2):333–45. [PubMed: 25060722]
51. Adams V, Bowen TS, Werner S, Barthel P, Amberger C, Konzer A, et al. Small-molecule-mediated chemical knock-down of MuRF1/MuRF2 and attenuation of diaphragm dysfunction in chronic heart failure. *J Cachexia Sarcopenia Muscle*. 2019.
52. Dominguez JF, Howell S. Compartmental analysis of steady-state diaphragm Ca<sup>2+</sup> kinetics in chronic congestive heart failure. *Cell Calcium*. 2003;33(3):163–74. [PubMed: 12600803]
53. Lindsay DC, Lovegrove CA, Dunn MJ, Bennett JG, Pepper JR, Yacoub MH, et al. Histological abnormalities of muscle from limb, thorax and diaphragm in chronic heart failure. *Eur Heart J*. 1996;17(8):1239–50. [PubMed: 8869866]

54. Jiang BH, Tardif JC, Shi Y, Dupuis J. Bosentan does not improve pulmonary hypertension and lung remodeling in heart failure. *Eur Respir J.* 2011;37(3):578–86. [PubMed: 20595149]
55. Pacheco DM, Silveira VD, Thomaz A, Nunes RB, Elsner VR, Dal Lago P. Chronic heart failure modifies respiratory mechanics in rats: a randomized controlled trial. *Braz J Phys Ther.* 2016;20(4):320–7. [PubMed: 27556388]
56. Del Rio R, Marcus NJ, Schultz HD. Carotid chemoreceptor ablation improves survival in heart failure: rescuing autonomic control of cardiorespiratory function. *J Am Coll Cardiol.* 2013;62(25):2422–30. [PubMed: 24013056]
57. Aukrust P, Ueland T, Lien E, Bendtzen K, Muller F, Andreassen AK, et al. Cytokine network in congestive heart failure secondary to ischemic or idiopathic dilated cardiomyopathy. *Am J Cardiol.* 1999;83(3):376–82. [PubMed: 10072227]
58. Levine B, Kalman J, Mayer L, Fillit HM, Packer M. Elevated circulating levels of tumor necrosis factor in severe chronic heart failure. *N Engl J Med.* 1990;323(4):236–41. [PubMed: 2195340]
59. Tsutamoto T, Hisanaga T, Wada A, Maeda K, Ohnishi M, Fukai D, et al. Interleukin-6 spillover in the peripheral circulation increases with the severity of heart failure, and the high plasma level of interleukin-6 is an important prognostic predictor in patients with congestive heart failure. *J Am Coll Cardiol.* 1998;31(2):391–8. [PubMed: 9462584]
60. Reid MB, Moylan JS. Beyond atrophy: redox mechanisms of muscle dysfunction in chronic inflammatory disease. *J Physiol.* 2011;589(Pt 9):2171–9. [PubMed: 21320886]
61. Chaillou T, Kirby TJ, McCarthy JJ. Ribosome biogenesis: emerging evidence for a central role in the regulation of skeletal muscle mass. *J Cell Physiol.* 2014;229(11):1584–94. [PubMed: 24604615]
62. Kirby TJ, Lee JD, England JH, Chaillou T, Esser KA, McCarthy JJ. Blunted hypertrophic response in aged skeletal muscle is associated with decreased ribosome biogenesis. *J Appl Physiol* (1985). 2015;119(4):321–7. [PubMed: 26048973]
63. van Hees HW, Ottenheijm CA, Granzier HL, Dekhuijzen PN, Heunks LM. Heart failure decreases passive tension generation of rat diaphragm fibers. *Int J Cardiol.* 2010;141(3):275–83. [PubMed: 19150150]
64. Stull JT, Kamm KE, Vandenboom R. Myosin light chain kinase and the role of myosin light chain phosphorylation in skeletal muscle. *Arch Biochem Biophys.* 2011;510(2):120–8. [PubMed: 21284933]
65. McNamara JW, Li A, Dos Remedios CG, Cooke R. The role of super-relaxed myosin in skeletal and cardiac muscle. *Biophys Rev.* 2015;7(1):5–14. [PubMed: 28509977]
66. Sweeney HL, Bowman BF, Stull JT. Myosin light chain phosphorylation in vertebrate striated muscle: regulation and function. *Am J Physiol.* 1993;264(5 Pt 1):C1085–95. [PubMed: 8388631]
67. Callahan LA, She ZW, Nosek TM. Superoxide, hydroxyl radical, and hydrogen peroxide effects on single-diaphragm fiber contractile apparatus. *J Appl Physiol.* 2001;90(1):45–54. [PubMed: 11133892]
68. Dutka TL, Mollica JP, Lamboley CR, Weerakkody VC, Greening DW, Posterino GS, et al. S-nitrosylation and S-glutathionylation of Cys134 on troponin I have opposing competitive actions on Ca(2+) sensitivity in rat fast-twitch muscle fibers. *Am J Physiol Cell Physiol.* 2017;312(3):C316–C27. [PubMed: 27974300]
69. Murphy RM, Dutka TL, Lamb GD. Hydroxyl radical and glutathione interactions alter calcium sensitivity and maximum force of the contractile apparatus in rat skeletal muscle fibres. *J Physiol.* 2008;586(8):2203–16. [PubMed: 18308823]
70. Koubassova NA, Bershtitsky SY, Tsaturyan AK. Effects of an Interchain Disulfide Bond on Tropomyosin Structure: A Molecular Dynamics Study. *Int J Mol Sci.* 2018;19(11).
71. Gross SM, Lehman SL. Accessibility of myofilament cysteines and effects on ATPase depend on the activation state during exposure to oxidants. *PLoS One.* 2013;8(7):e69110. [PubMed: 23894416]
72. Walsh TP, Wegner A. Effect of the state of oxidation of cysteine 190 of tropomyosin on the assembly of the actin-tropomyosin complex. *Biochim Biophys Acta.* 1980;626(1):79–87. [PubMed: 6893942]

73. Dalle-Donne I, Rossi R, Giustarini D, Gagliano N, Di Simplicio P, Colombo R, et al. Methionine oxidation as a major cause of the functional impairment of oxidized actin. *Free Radic Biol Med*. 2002;32(9):927–37. [PubMed: 11978495]
74. Prochniewicz E, Lowe DA, Spakowicz DJ, Higgins L, O'Connor K, Thompson LV, et al. Functional, structural, and chemical changes in myosin associated with hydrogen peroxide treatment of skeletal muscle fibers. *Am J Physiol Cell Physiol*. 2008;294(2):C613–C26. [PubMed: 18003749]
75. Balog EM, Norton LE, Bloomquist RA, Cornea RL, Black DJ, Louis CF, et al. Calmodulin oxidation and methionine to glutamine substitutions reveal methionine residues critical for functional interaction with ryanodine receptor-1. *J Biol Chem*. 2003;278(18):15615–21. [PubMed: 12586832]
76. Fedorova M, Kuleva N, Hoffmann R. Identification of cysteine, methionine and tryptophan residues of actin oxidized in vivo during oxidative stress. *J Proteome Res*. 2010;9(3):1598–609. [PubMed: 20063901]
77. Tiago T, Ramos S, Aureliano M, Gutierrez-Merino C. Peroxynitrite induces F-actin depolymerization and blockade of myosin ATPase stimulation. *Biochem Biophys Res Commun*. 2006;342(1):44–9. [PubMed: 16480685]

**Highlights**

- HFrEF causes diaphragm weakness differentially in moderate and severe disease.
- Ribosomal and glycolytic metabolism proteins decrease in abundance in severe HFrEF.
- Heightened cysteine and methionine oxidation occurs in thin filament proteins in severe HFrEF.



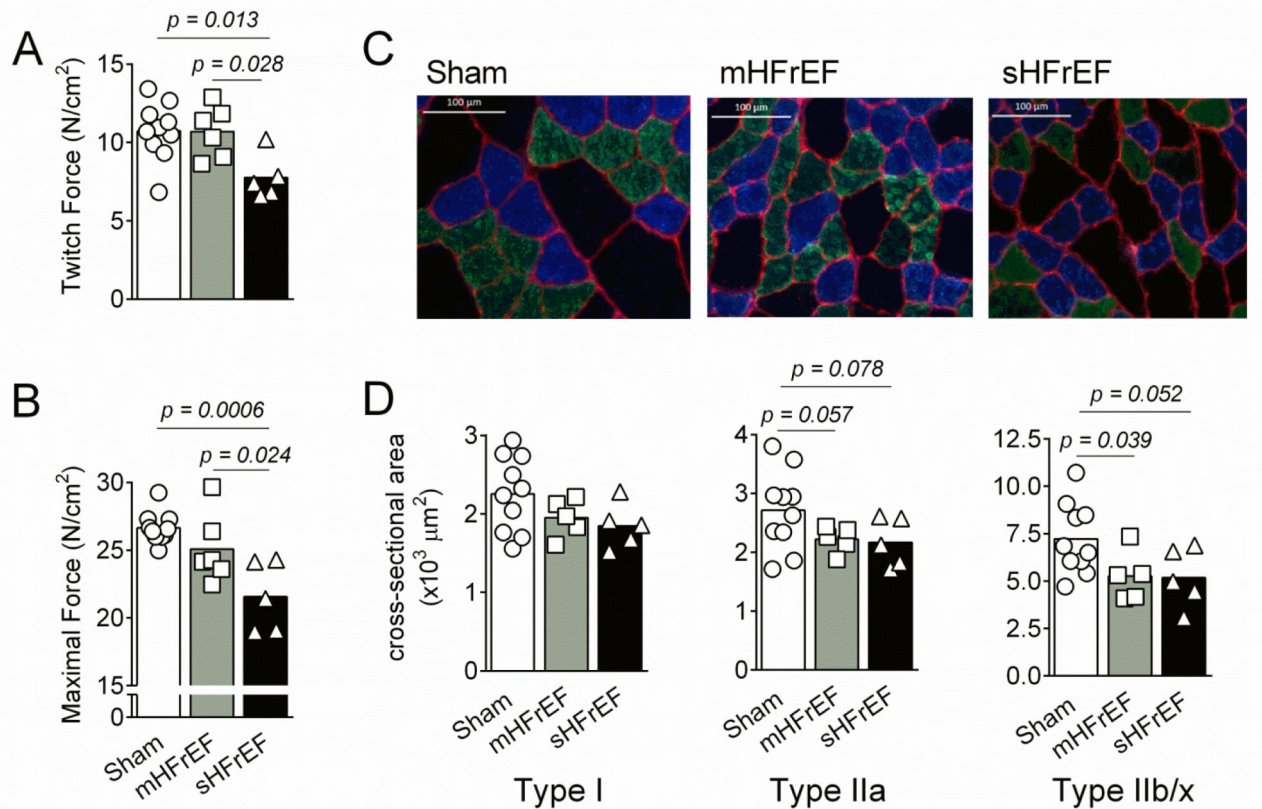


**Figure 1. Isometric diaphragm contractile function, fiber cross-sectional area, and fiber type distribution.**

A) Twitch force (1 Hz, field stimulation). B) Maximal force (120 Hz, field stimulation). In panels A and B, scatter plots show data from each animal. Bars represent group means. Statistical analysis by one way ANOVA (twitch force:  $F[2, 18] = 5.75$ ,  $p = 0.017$ ; maximal force:  $F[2, 18] = 10.78$ ,  $P = 0.0008$ ) and Tukey's post-hoc comparison. C) Sample images of immunohistochemistry for fiber typing and cross-sectional area. Colors represent specific MHC isoforms (blue = type I, green = type IIa, black = type IIb/x). Statistical analysis by linear mixed model. D) Cross-sectional area for each fiber type. Type I fibers did not reach the threshold for statistical significance in mHFrEF ( $p = 0.12$ ) and sHFrEF ( $p = 0.11$ ) compared to Sham. Scatter plots show average value of individual fibers measured for each animal. Bars represent group means.

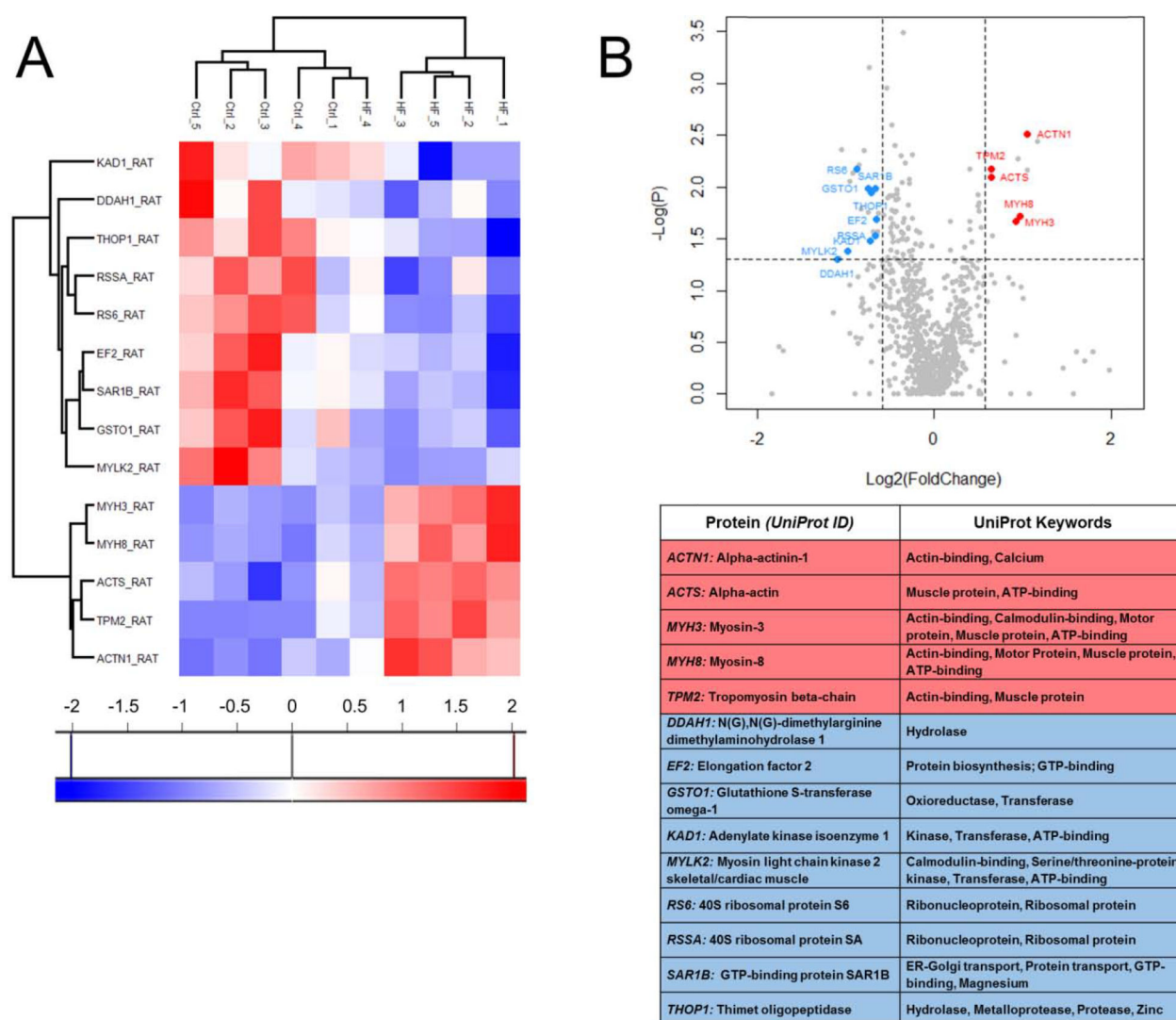


**Figure 2. Relative fold change in protein abundance determined by label-free proteomics.**

A) Significantly changed proteins that met criteria of  $p < 0.05$  ( $-\text{Log}P > 1.3$ ),  $>1.5$  fold change ( $-0.585 < \text{Log}_2 > 0.585$ ), and at least three unique peptides are highlighted in red (up regulated) and blue (down regulated). B) Volcano plot shows distribution of proteins identified in diaphragm from Sham and HFREF animals. Proteins in the top left and right corners met the criteria for down and upregulation, respectively. Select proteins are labeled in the figure and listed in the accompanying table.

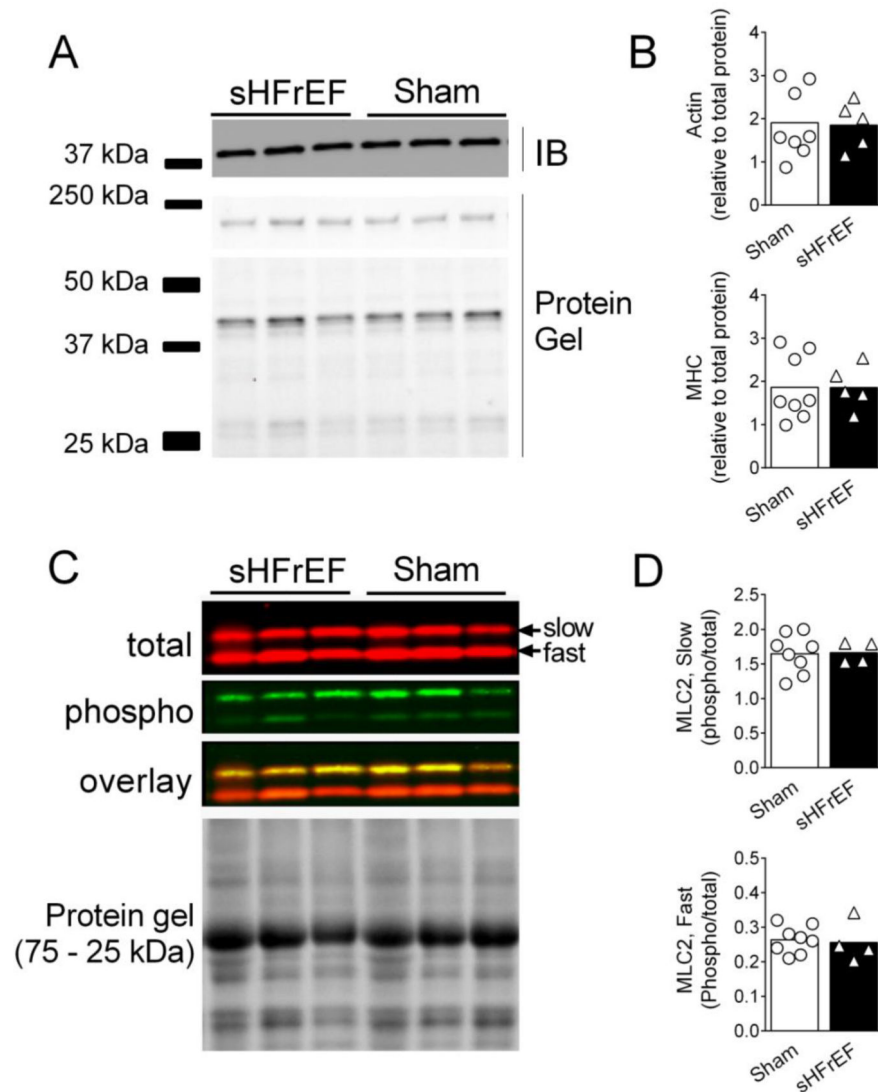


**Figure 3. Abundance of myosin heavy chain (MHC), actin, and phosphorylation status of myosin regulatory light chain (MLC2).**

A) Sample image of actin immunoblot (IB) and MHC gel. The stain-free gel image shows MHC band (~220 kDa, top) and protein abundance in the molecular weight range of 25 to 50 kDa. Top and bottom portions of stain-free gel are from same gel and were split to facilitate visualization of bands of interest for MHC and actin. B) Actin and MHC abundance. C) Sample immunoblot images of total and phosphorylated MLC2. Diaphragm homogenates show both fast and slow isoforms of MLC2. D) Phosphorylation status of each MLC2 isoform (phospho/total MLC2).

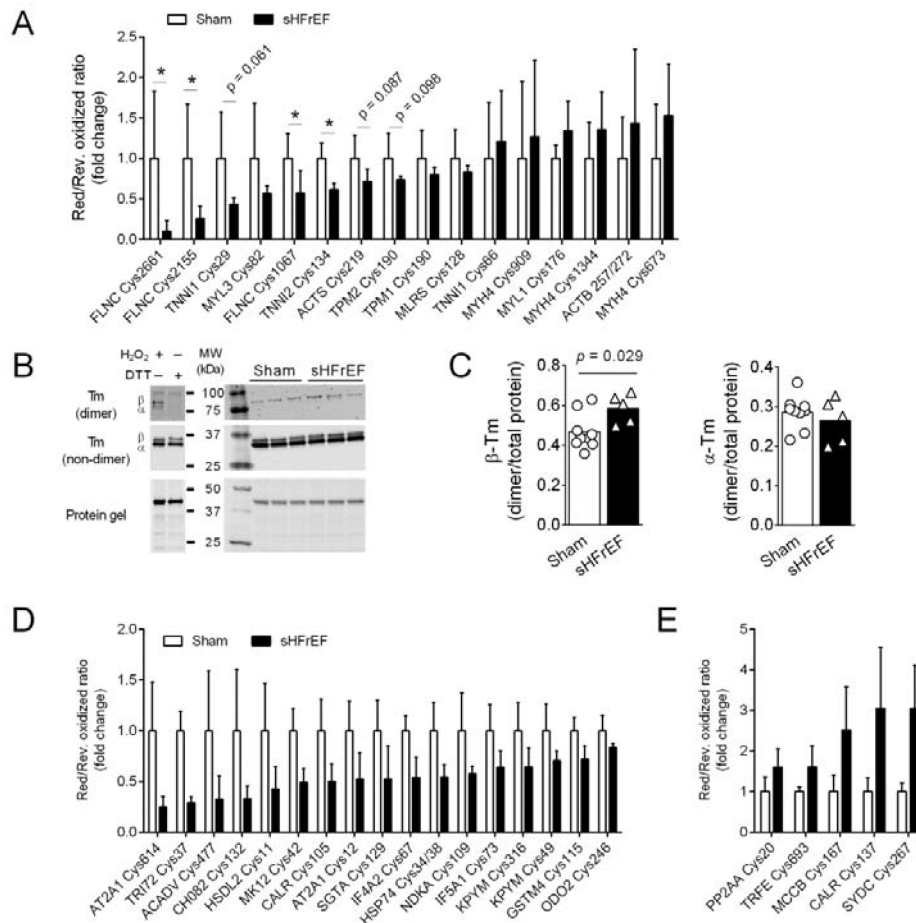


**Figure 4. Redox state changes of cysteine in sHFrEF.**

A) Cysteine redox state of myofibrillar and structural proteins. Data are fold change in ratio intensity of reduced/reversibly oxidized. Open bars (□): Sham, closed bars (■): sHFrEF. Data are normalized to average of Sham and arranged from left to right in ascending order based on mean values for sHFrEF. Bars show mean data and error bars are standard deviation. The data show shifts toward more oxidized (decrease in ratio) and reduced state (increase in ratio) in sHFrEF. *P*-values less than 0.05 (\*) and 0.10 are indicated in the figure. All exact *p*-values are shown in Table 2. B) Tropomyosin oxidation detected by non-reducing gel and immunoblot. Top and middle are sample immunoblot images, bottom is protein abundance from stain-free gel. Left side, positive and negative controls; right side, samples from Sham and sHFrEF groups. C) Scatter plot and mean (bars) data from dimerized β-Tm (Tpm2, fast) and α-Tm (Tpm1, slow) isoforms. (D-E) Cysteine redox state of non-myofibrillar proteins that changed significantly in sHFrEF. Data are fold change (normalized to average of Sham) in ratio intensity of reduced/reversibly oxidized Cys residues. Panels are arranged based on Cys residues (and proteins) with shift toward more oxidized (panel D) and reduced state (panel E) in sHFrEF. Bars show mean data and error bars are standard deviation. All comparisons shown in panels D and E reached statistical significance (*p* < 0.05). Exact *p*-values are shown in Table 3.

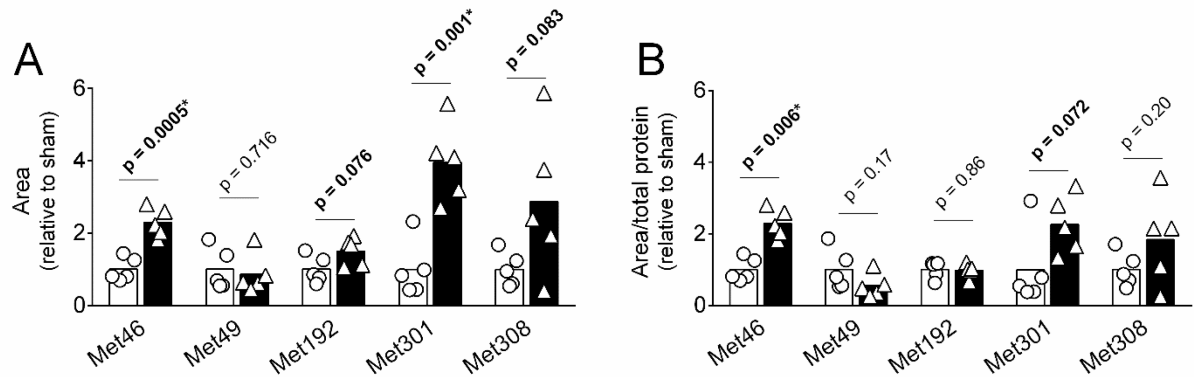


**Figure 5. Oxidized methionine residues in skeletal muscle  $\alpha$ -actin.**

Data are fold change (normalized to average of Sham) in sum of area of precursor ion, precursor + M1, and precursor + M2 (Panel A) and sum of area normalized to total skeletal muscle  $\alpha$ -actin (ACTS) abundance from global proteomics (Panel B). Bars show mean and symbols are individual data from Sham (white bar, circles) and sHFrEF (black bar, triangles).

**Table 1.**

Animal characteristics.

	Sham (n = 10)	mHFrEF (n=6)	sHFrEF (n=5)	<i>p</i> -value		
				Sham vs mHFrEF	Sham vs sHFrEF	mHFrEF vs sHFrEF
Fractional shortening (%)	50 ± 6	28 ± 7	27 ± 8	0.0003	0.0009	0.952
Infarct area (%)	-	26 ± 6	43 ± 3	-	-	0.0004 *
RV weight (mg)	316 ± 35	334 ± 60	490 ± 126	>0.999	0.010	0.051
LV weight (mg)	1090 ± 87	1114 ± 98	1047 ± 53	<i>p</i> = 0.897 (one way Anova)		
Tibia length (mm)	44 ± 1.4	44 ± 2	44 ± 1	<i>p</i> = 0.679 (one way Anova)		
RV weight/TL (mg/mm)	7.1 ± 0.7	7.6 ± 1.3	11.2 ± 3.1	>0.999	0.009	0.069
LV weight/TL (mg/mm)	25 ± 2	25 ± 2	24 ± 1	<i>p</i> = 0.368 (one way Anova)		
Body weight (initial, g)	271 ± 30	271 ± 27	241 ± 22	<i>p</i> = 0.131 (one way Anova)		
Body weight (final, g)	692 ± 50	652 ± 40	630 ± 41	0.217	0.054	0.715
BNP (pg/ml)	88 ± 51	278 ± 243	401 ± 241	0.474	0.021	0.610

Data are mean ± SD. Statistical analysis by One way ANOVA with Tukey's post-hoc test for all variables except RV weight, RV weight/TL and BNP, which were analyzed by Kruskal-Wallis ANOVA with Dunn's post-hoc test. Infarct area compared using student's t-test. RV = right ventricle; LV = left ventricle; BNP = Brain natriuretic peptide. Experiments were completed 15–17 weeks post-surgery.

\* Student's t-test.



**Table 2.**

List of myofilament and structural proteins containing redox-sensitive cysteine residues detected by redox proteomic approach.

accession	protein	Abundance (HFrEF/Sham)	p-value (abundance)	Cys residue	Sham (red/ox)	HFrEF (red/ox)	p-value (red/ox)
P68136	ACTS: Actin, alpha skeletal muscle	<b>1.56</b>	<b>0.008</b>	219	9.7	6.9	0.087
P60711	ACTB: Actin, cytoplasmic 1	<b>1.41</b>	<b>0.015</b>	287 257/272	8.6 34.5	7.0 49.5	0.215 0.381
D3ZHA0	FLNC: Filamin-C	<b>0.79</b>	<b>0.02</b>	1067 1915 2155 2661	0.05 32.8 40.8 7.2	0.03 78.07 10.4 0.7	0.050 0.31 0.043 0.043
P04466	MLR3: Myosin regulatory light chain 2	<b>1.32</b>	<b>0.006</b>	128	27.0	22.4	0.323
P16409	MYL3: Myosin light chain 3	1.25	0.28	81 403	30.3 4.5	17.3 6.9	0.203 0.238
Q29RW1	MYH4: Myosin heavy chain 2b	1.26	0.06	909	2.1	2.6	0.665
P02600	MYL1: Myosin light chain 1/3	0.85	0.76	1344 176	9.1 5.7	12.4 3.7	0.253 0.385
P13413	TNNI1: Troponin I, slow	1.42	0.12	29 66	63.2 23.5	27.4 28.5	0.061 0.625
P27768	TNNI2: Troponin I, fast	<b>1.42</b>	<b>0.014</b>	134	12.0	7.4	0.003
P04692	TPM1: $\alpha$ -Tropomyosin, slow	1.42	0.12	190	10.8	8.7	0.249
P58775	TPM2: $\beta$ -Tropomyosin, fast	<b>1.57</b>	<b>0.006</b>	190	9.7	7.1	0.098

Data include changes in protein abundance from label-free quantification and redox ratio of individual Cys residues within those proteins. Proteins highlighted in bold have a significant change in abundance between diaphragm from Sham and HFrEF rats. P-values are for comparison between ratios of reduced/reversibly oxidized Cys. A decrease in the ratio indicates elevated oxidation in HFrEF. Mean  $\pm$  SD of data normalized to average of Sham are shown in Figure 4.

**Table 3.**

List of general proteins with significant change in ratio of reduced/reversibly oxidized Cys residues.

accession	protein	Abundance (HFrEF/Sham)	P-Value (abundance)	Cys residue	Sham (red/ox)	HFrEF (red/ox)	P-value (red/ox)
<b>Q5RKL1</b>	<b>Eukaryotic initiation factor 4A-II</b>	<b>0.74</b>	<b>0.017</b>	67	11.0	5.9*	0.003
<b>Q63538</b>	<b>Mitogen-activated protein kinase 12</b>	<b>0.78</b>	<b>0.009</b>	42	0.4	0.2*	0.002
Q01205	Dihydropyridyllysine-residue succinyltransferase component of 2-oxoglutarate dehydrogenase complex	1.13	0.28	246	8.4	7.1*	0.047
<b>P19804</b>	<b>Nucleoside diphosphate kinase B*</b>	<b>0.8</b>	<b>0.024</b>	109	4.9	2.8*	0.038
P18418	Calreticulin	0.87	0.28	105	0.3	0.1*	0.014
				137	0.1	0.4	0.018
O70593	Small glutamine-rich tetrapeptide repeat-containing protein alpha	0.79	0.76	129	0.3	0.2*	0.045
<b>P08009</b>	<b>Glutathione S-transferase Yb-3</b>	<b>0.84</b>	<b>0.04</b>	115	8.4	6.1*	0.011
<b>P11980</b>	<b>Pyruvate kinase PKM</b>	<b>0.66</b>	<b>0.05</b>	49	17.4	12.3*	0.049
				326	3.9	2.5*	0.044
P63331	Serine/threonine-protein phosphatase 2A catalytic subunit alpha isoform	0.88	0.11	20	4.3	6.8	0.048
Q4V8F9	Hydroxysteroid dehydrogenase-like protein 2	0.86	0.22	11	0.5	0.2*	0.038
A0JPQ4	Tripartite motif-containing protein 72	0.83	0.61	37	0.5	0.2*	0.000
Q64578	Sarcoplasmic/endoplasmic reticulum calcium ATPase 1	0.89	0.62	12	7.7	4.0*	0.026
				614	3.0	0.8*	0.009
P15178	Aspartate-tRNA ligase, cytoplasmic	1.06	0.33	267	2.3	7.0	0.003
Q5XIT9	Methylcrotonoyl-CoA carboxylase beta chain, mitochondrial	1.23	0.09	167	1.5	3.7	0.018
P45953	Very long-chain specific acyl-CoA dehydrogenase, mitochondrial	1.0	0.98	477	284.0	92.6*	0.045
P12346	Serotransferrin	0.81	0.14	693	0.07	0.11	0.037
O88600	Heat shock 70 kDa protein 4	1.19	0.15	34/38	1.0	0.5*	0.010
Q642A4	UPF0598 protein C8orf82 homolog	1.0	0.98	132	12.6	4.2*	0.042
<b>Q3T1J1</b>	<b>Eukaryotic translation initiation factor 5A-1</b>	<b>0.79</b>	<b>0.02</b>	73	2.8	1.8*	0.029

Data include changes in protein abundance from label-free quantification and redox ratio of individual Cys residues within those proteins. Proteins highlighted in bold have a significant change in abundance between diaphragm from Sham and HFrEF rats. P-values are for comparison between ratios of reduced/reversibly oxidized Cys. A decrease in the ratio, shown by an asterisk, indicates elevated oxidation in HFrEF. Mean  $\pm$  SD of data normalized to average of Sham are shown in Figure 4.